Influence of absorber layer dopants on performance of Ge/Si Single Photon Avalanche Diodes

Neil J. Pilgrim,[1, a)] Zoran Ikonic,[1] and Robert W. Kelsall[1]

Institute of Microwaves & Photonics, University of Leeds, Leeds,

UK

Monte Carlo electronic transport simulations are applied to investigate the influence of the Ge absorber layer on the performance of Ge/Si single photon avalanche diodes (SPADs). Ge dopant type and concentration control the internal electric field gradients, which directly influence the probabilistic distribution of times from the point of charge photo-generation to that of transmission over the Ge/Si heterojunction. The electric field adjacent to the heterointerface is found to be the dominant factor in achieving rapid transmission, leading to a preference for p-type dopants in the Ge absorber. The contribution to jitter from the Ge layer is estimated and appears relatively independent of bias, though scales near-linearly with layer height.

---

a)Electronic mail: dr.n.pilgrim@kepier.clara.net

I. INTRODUCTION

Detection of very low amplitude optical signals down to the single-photon regime is becoming of increasing interest[1], with application areas including quantum computing and cryptography[2,3], biophotonics[4], laser ranging and imaging[5] and semiconductor circuit diagnostics[6]. One approach for measuring such signals involves adapting an avalanche photodiode (APD) device and operating it in a Geiger (trigger-reset) mode, the resulting device being commonly known as a single-photon avalanche diode (SPAD)[7]. SPADs have been developed from a range of different semiconductor materials, with the most successful being developed either from solely Si[7] or from a heterostructure comprising III-V semiconductors such as InGaAs/InP[8]. The former have benefited hugely from existing manufacturing infrastructure, and integration opportunities have led to the fabrication of arrays of SPADs alongside CMOS logic[9]. However, as is well known, Si suffers from poor optical absorption properties, a negative impact which is particularly noticeable in detection efficiences at longer wavelengths towards the near infrared. On the contrary, III-V semiconductor SPADs are far more capable when working within this spectral region, and the variety of heterostructure designs which are possible enables device optimisation to achieve low-noise absorption at longer wavelengths coupled with efficient multiplication.

Inspired by the added flexibility afforded by the inclusion of Ge or SiGe alloys into CMOS, the area of silicon photonics has undergone significant recent development, with the narrower band-gap Ge providing scope for significant improvements in optical absorption compared to pure Si devices, particularly around the two main telecommunications wavelengths of $1.3 \, \mu m$ and $1.55 \, \mu m$. This capability has led to the development of various long-wavelength photodetectors, including Ge/Si APDs in both nanoscale[10] and traditional[11] architectures. We select the latter device architecture for operation as a SPAD, due to its similarity to III-V heterostructure SPAD designs, where band-to-band tunnelling is minimised by maintaining the electric field at a low level in the narrow band-gap absorption material. This is expected to avoid the problems found previously when operating pure Ge APDs in Geiger mode[12,13], where $77 \, K$ operation was necessary in order to limit dark counts, but which also lowered the maximum wavelength detected to less than $1.5 \, \mu m$. This design approach is supported by epitaxial techniques which allow the growth of Ge directly on Si with only a small residual thermal strain and relatively low defect densities[14,15].

The aim of this work is to explore Ge/Si structures which might be suitable for operation as SPADs, through the application of a Monte Carlo transport model to simulate the device dynamics, considering which design parameters are likely to lead to designs with the highest performance. We specifically focus on the Ge absorption layer, due to the potential impact of unintentional dopants on device efficiency.

II. SPAD DESIGN & MODELLING APPROACH

Following an absorption event in the Ge layer, an avalanche in a Si layer might be triggered by either one of the photogenerated carriers. However, based on the asymmetry in the impact ionization coefficients within Si[16], our analysis has initially focused upon triggering avalanches via electrons. To achieve the appropriate orientation of electric fields (under reverse biasing) requires an overall p-i-n design, with a p$^+$ top Ge contact layer and an n$^+$ Si bottom contact layer. In order to optimize the electric fields within each material a separate absorption, charge and multiplication (SACM or SAM) layer scheme may be followed, resulting in a p$^+$-i-p-i-n$^+$ doping profile within the epitaxial layers, as illustrated schematically in figure 1.

There are two key elements to consider when examining the performance of SPAD devices. The first is the non-optical source of measured events, the dark count rate (DCR), which must be maintained as low as possible. The origin of the DCR is typically a balance between band-to-band tunnelling (at high electric fields), defect-assisted tunnelling (at high defect densities) and generation-recombination mechanisms (at high temperature)[17]. Only the first of these may be controlled through device design and would be most significant in the narrow band-gap Ge absorption layer. The second element is the need for a sufficiently high photon detection efficiency (PDE): the quantum efficiency must be sufficiently great so as to produce an electron-hole pair from an incident photon, and the device must then efficiently convert that charge into a measurable current pulse. Factors contributing to the PDE may be subdivided according to the route the signal takes through the device: initial charge generation, charge transport to the point of impact-ionization, and sustained avalanche to the point where the current may be measured. The transport in the Ge layer connecting the charge generation and avalanche processes is potentially a significant bottleneck due to the presence of the heterointerface and associated potential barriers. Based on the above, we
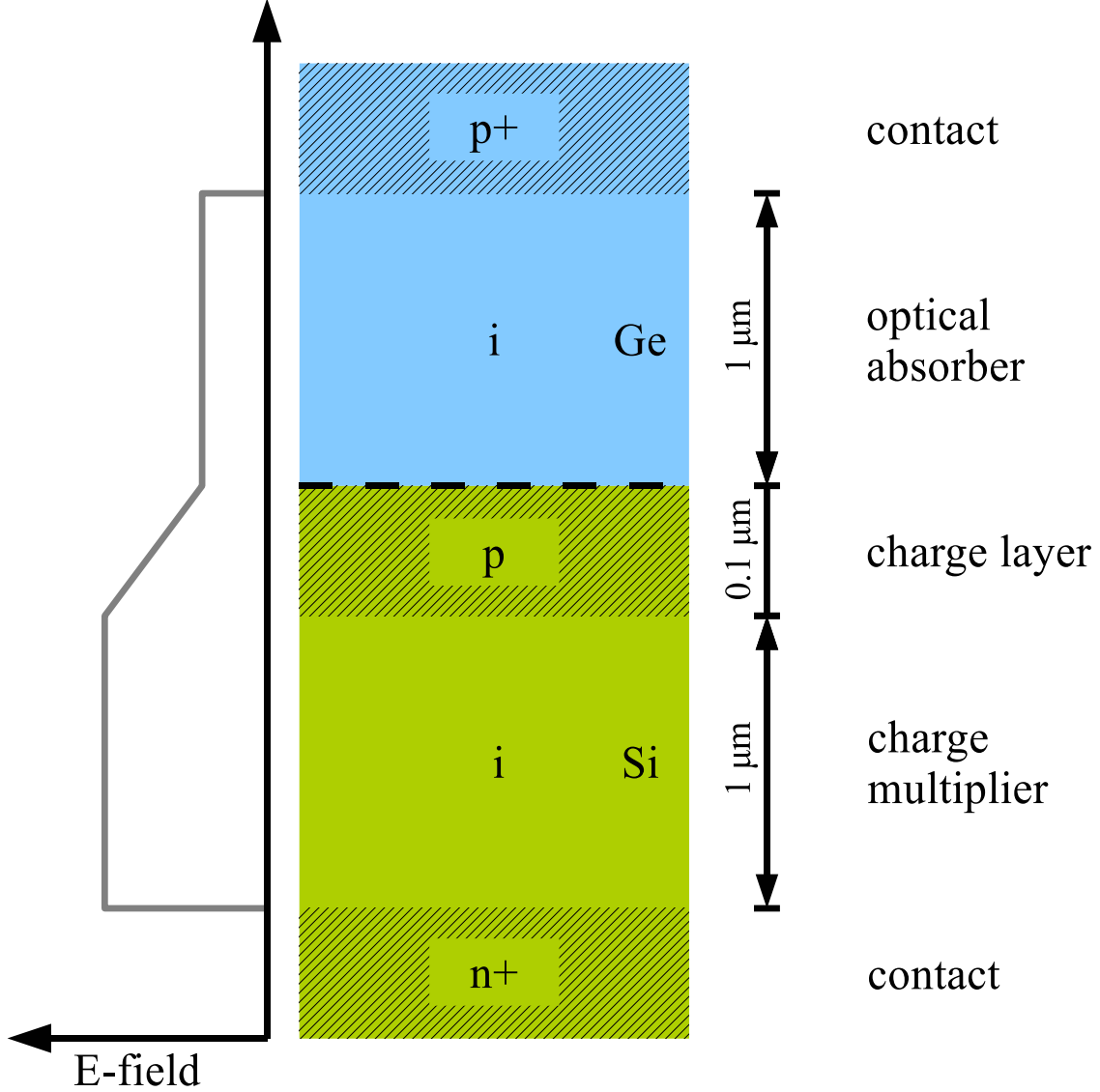
FIG. 1. Schematic diagram of an idealised p$^+$-i-p-i-n$^+$ device and the corresponding electric field profile; real devices have finite unintentional doping in the regions marked as intrinsic.

have elected to focus our analysis upon the Ge absorption layer, considering the time from charge generation to entry of that charge into the Si charge layer.

The charge transport model chosen follows an established Monte Carlo approach[18], our implementation of which we have developed and applied over a number of years[19–22] and now extended to Ge. Since the SPAD operates in a heavily reverse-biased mode and is essentially depleted of mobile charge except during avalanche, only electron transport is included because the device relies upon these carriers for avalanche triggering in the Si layers. Analytical expressions are used to approximate the Ge bandstructure as non-parabolic

ellipsoidal energy surfaces around the L and Δ symmetry locations. Parameters for the bandstructure and many of the carrier-phonon scattering processes are taken from a fit to transport measurements[23]. One exception is made for the scattering deformation potentials between the Γ and other minima, for which fits to transport measurements do not provide a highly constrained range of values; instead values from optical measurements are used[24]. The energy offsets between the valley minima incorporate the small residual strain ($\approx 0.18\%$) from growth of Ge on Si[15], causing a small energy splitting of the Δ minima into the Δ_2 pair and Δ_4 quadruplet and other small energy shifts[25,26]. Simulations are performed assuming an ambient temperature of $300\,\mathrm{K}$.

In addition to the use of the Monte Carlo method for transport, a random sampling approach is also used to account for the random locations of charge generation within the Ge layer. Light of a given single wavelength is assumed to impinge upon the top surface of the Ge, with a decaying probability of generation over the depth of the layer based on the Beer-Lambert expression. The absorption coefficient is taken for Ge with the small residual strain from after-growth cooling as indicated above[27], which for an incident wavelength of $1.55\,\mu\mathrm{m}$ results in a spatial distribution of carriers which is relatively homogeneous. To simplify the collection of statistics a large ensemble of generated electrons (up to 500,000) is simulated synchronously, enabling probability distribution data to be easily collected as a function of time. The ensemble is generated with a thermal distribution within the Γ minimum, representing the dominance of direct absorption and neglecting any excess photon energy above the direct band gap.

As noted above, since the device may be considered to have a negligible amount of mobile charge present during the simulated period (prior to significant sustained avalanching), then a simple non-self-consistent fixed electric field profile is sufficient. The Monte Carlo transport algorithm is then applied to the large ensemble of particles representing the electrons, in timesteps of $1\,\mathrm{fs}$, until all particles exit the simulation or a very long simulation time has elapsed (typically $2\,\mathrm{ns}$).

Particles may exit from the simulation upon reaching the top or bottom of the simulated Ge absorption layer, primarily the latter at the heterointerface due to the electric fields in the simulation domain. This interface behaves similarly to a non-injecting Schottky contact in a typical Monte Carlo transport simulation[28]. However, it also incorporates the required dynamics of a heterojunction: selectively accepting or rejecting (transmitting or

reflecting) incident particles based on their momentum upon reaching the interface. The potential barriers experienced by an electron in the Ge L or Γ minima are determined through application of a theoretical value for the Si-Ge average valence band energy offset of $0.47\,\text{eV}$[29], in combination with the established unstrained Si band offsets at $300\,\text{K}$.

The transmission across the heterointerface is primarily determined according to the relative energy of the incident electron and any energy barrier for the valley within which the electron resides at that moment, in the standard semiclassical manner. In addition, two tunnelling mechanisms have been examined: direct tunnelling and phonon-assisted tunnelling. Direct tunnelling was calculated through application of WKB theory and a triangular approximation to the barrier shape, with barrier height determined dynamically in each case based on a comparison of the energy of the impinging electron with the heterojunction conduction-band energy offset. Phonon-assisted tunnelling was considered by calculating a probability according to the dwell time in the barrier multiplied by an appropriate intervalley scattering. The dwell time in the barrier was determined numerically[30], using an approach which is consistent with the WKB result for the triangular barrier tunnelling probability. The scattering rate was determined in an analogous way to regular intervalley scattering within a single material, but with one of the energy levels (minima) involved being taken from the other material. The transitions considered were those close in energy to one another: transitions in Ge from Γ and L valley states into lower-lying states corresponding to the Si Δ valleys, and transitions in Si from upper-lying states corresponding to the Ge Γ and L valleys into the real Si Δ valley states. The latter correspond to electronic states in Ge extending into the Si layer, from which scattering is then possible into the real Δ states; the former corresponds to scattering from real states within Ge into the evanescent tail of the Si Δ states.

III.   RESULTS

The absolute applied external bias is not important when modelling only the Ge absorption layer, since potential drops occur across other device layers according to their doping density profiles. Consequently, rather than considering application of specific external biases, instead various electric field profiles within the Ge absorption layer (perpendicular to the epilayers) were investigated.
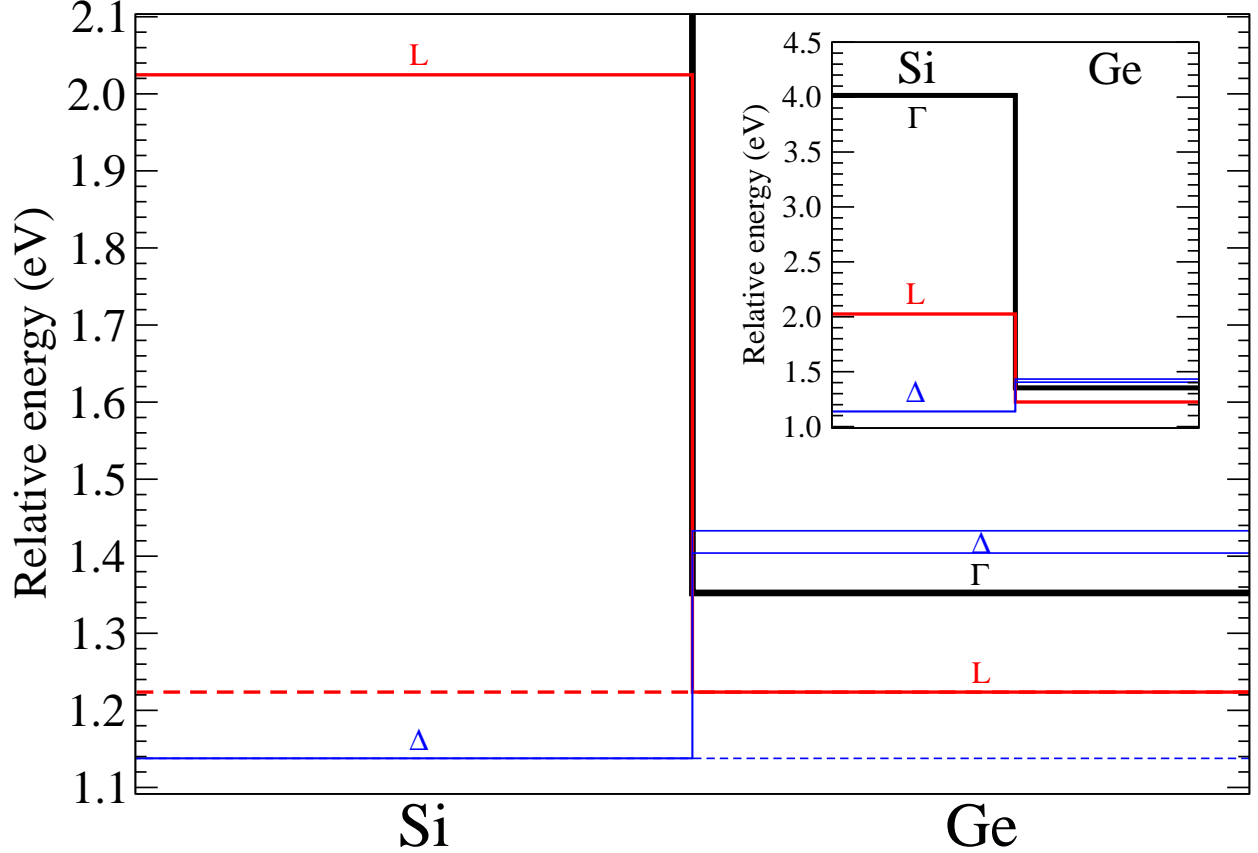
6

FIG. 2. Relative conduction-band offsets between Si and lightly-strained Ge in the flat-band case, highlighting the potential barriers for electrons traversing from Ge into Si in the L or Γ minima. Solid lines indicate real states, dashed lines correspond to energies relevant for phonon-assisted tunnelling (L and Δ states only). Inset: full range of real energy minima modelled.

A. Just-active absorption layer

At low applied biases the transfer of electrons photo-generated in the Ge layer across the heterointerface into the Si multiplication layer is severely impeded. If the background doping is p-type, this occurs since the Ge layer is not fully depleted, causing transport to the heterointerface to rely upon slow diffusion; if the background doping is n-type, the electric field near the interface opposes transport in this region. As the bias is raised, an increasing depth of the Ge absorption layer becomes active - namely having a finite electric field and able to drift photogenerated electrons in the direction of the heterointerface. The first operating point we consider is at the bias where the entire Ge absorption layer is *just active*; this is expected to correspond to the minimum operating bias. At this point, neglecting edge

effects due to the Ge contact homojunction, the electric field profile runs from zero at one end of the layer to a finite value at the other, the latter determined by the intervening net background doping. The background doping is assumed to be uniform, of p- or n-type, and fully ionized, with densities of approximately $10^{15}\,\mathrm{cm^{-3}}$ to $10^{16}\,\mathrm{cm^{-3}}$. At the bias where the Ge layer is just active, the electric field in the Ge layer is easily calculated from electrostatics to be given by

$$\Delta E = 1.13 \times 10^{-9} NL \tag{1}$$

where ΔE is the shift in electric field over the height L of Ge layer, with a doping N. Substituting in a layer height of $1.0\,\mu\mathrm{m}$ and the above doping density range gives peak electric fields of $1.13 \times 10^6\,\mathrm{V\,m^{-1}}$ to $1.13 \times 10^7\,\mathrm{V\,m^{-1}}$. Simulations have been performed with electric field profiles which vary linearly by $10^6\,\mathrm{V\,m^{-1}}$ to $10^7\,\mathrm{V\,m^{-1}}$ over $1\,\mu\mathrm{m}$ and are shown in figure 3.

Figure 4 shows the temporal characteristics when the absorption layer is just active, obtained by tracking the probability that a given fraction of the original ensemble of electrons remains in the Ge layer as a function of time. Four lines are shown, for n-type (solid) and p-type (dotted) background doping in the Ge absorber layer, each with densities of $10^{15}\,\mathrm{cm^{-3}}$ and $10^{16}\,\mathrm{cm^{-3}}$. Ideally these lines should drop to zero as rapidly as possible, indicating that electrons photo-generated in the Ge layer are rapidly and efficiently emptied into the Si layer, such that avalanche multiplication can occur as rapidly as possible. In addition to being directly relevant to the speed of the device, if electrons do not rapidly exit into the Si layer then they are more likely to be affected by undesirable mechanisms in the Ge, such as trapping and recombination.

It is clear from the figure that electrons will spend markedly less time in a p-type Ge layer than an n-type Ge layer, and that for each type of doping, a higher doping density also reduces the time spent in the Ge layer. The latter point is clearly related to the enhanced energy transfer to the electrons from the higher electric field over the entire thickness of the Ge layer, leading to a higher probability that upon reaching the heterointerface an electron will either be in a Δ state (with no energy barrier), or else be in an L state and have sufficient energy to transfer over the potential barrier. The only change in the electric field profile between p-type and n-type doping in the just-active case is as depicted in figure 3, with the p-type profile having the highest electric field near the heterointerface and being zero at the top of the layer, whereas the n-type profile has the opposite trend. This suggests that
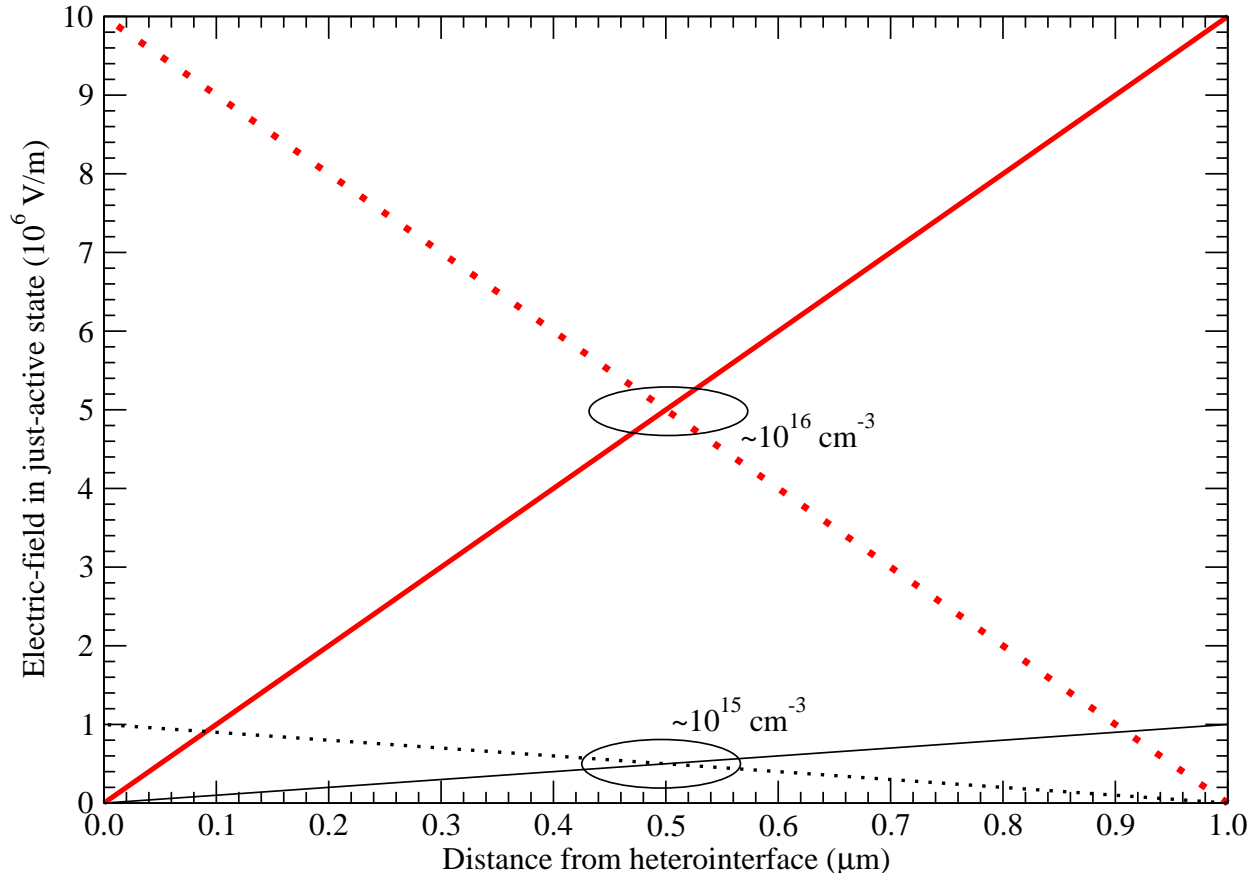
8

FIG. 3. Electric field profiles within the Ge absorber layer as a function of the distance from the Ge/Si heterointerface, for p-type (dotted) and n-type (solid) doping of $10^{15}\,\mathrm{cm}^{-3}$ (thin/black lines) and $10^{16}\,\mathrm{cm}^{-3}$ (thick/red lines), when the layer is just-active.

the improvement in transit-time characteristics associated with switching to p-type dopants may be related to the electric field being at its peak close to the interface rather than at the top of the device. For an n-type Ge layer, the high electric field transfers more energy to the electrons the further they are from the heterointerface - yet when far from the interface they have a greater distance in which to lose that energy to the lattice. For p-type Ge the situation is reversed and improved, since the largest energy input to the electrons takes place near the interface, where the electrons will (if they transfer over sufficiently quickly) spend little time and stand little chance of being cooled by the lattice.

This explanation is supported by figure 5, which shows the energy dissipated to the lattice (by sampling the net phonon emission[19]) over the course of each of the simulations shown in figure 4. For p-type doping (dotted lines) there is a gradual increase in energy dissipa-
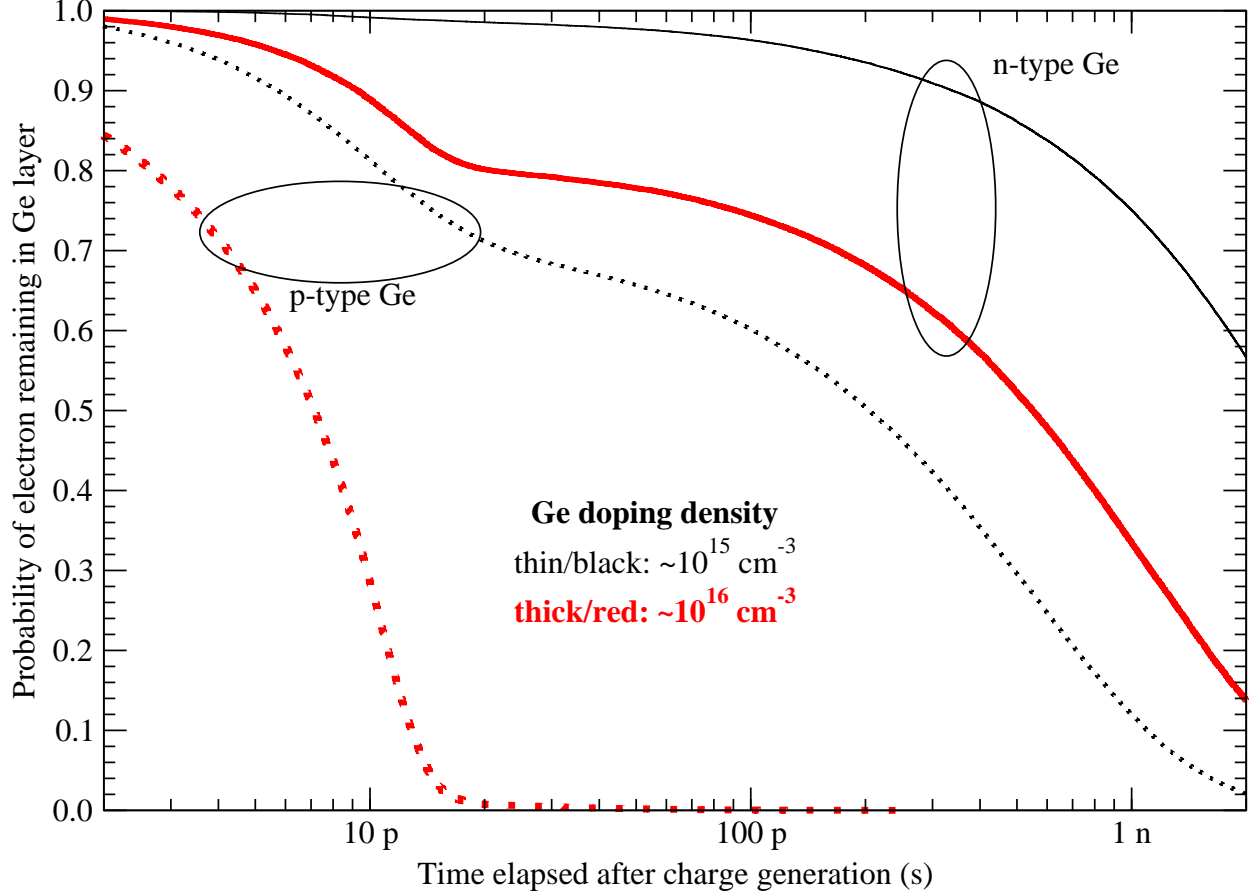
FIG. 4. Probability of a photo-generated electron remaining in a just-active Ge absorption layer as a function of time, characterising the transmission over the Ge/Si heterointerface. Doping type and density combinations are as in figure 3: p-type (dotted) and n-type (solid); $10^{15}\,\mathrm{cm}^{-3}$ (thin/black lines) and $10^{16}\,\mathrm{cm}^{-3}$ (thick/red lines).

tion towards the interface, in line with the increasing electric field and also the aggregate contribution arising from increasing numbers of electrons which pass through locations close to the interface. For n-type doping, maximum dissipation occurs in the centre of the Ge absorption layer. While this distribution of energy dissipation within the Ge absorption layer should not influence the transport characteristics in the case of single photon operation, it is interesting to compare the curves in figure 5 and 4. The inefficiencies of n-type doping are emphasised through comparison of the highly-doped (thick/red) n-type (solid) and p-type (dotted) results in these two figures: on average for the case of n-type doping there is significantly more energy dissipation from electrons to the lattice, whilst this case also exhibits lower transport efficiencies.

An additional trend apparent in figure 4 is the presence of two timescales, broadly on either side of 10 ps to 20 ps. At durations shorter than this characteristic time, transport is understood to be dominated by an initial transfer of the hot-energy tail of electrons photogenerated anywhere within the Ge absorption layer over the heterointerface. Any remaining electrons accumulate adjacent to the interface until they gain sufficient energy (by phonon absorption) or are transferred into the Δ minima in which there are no energy barriers for transfer into the Si layer. In some cases (upper curve in figure 4) the latter process appears to dominate, while in others (lower curve in same figure) it is the former. The presence of the latter process may also be observed in figure 5 as peaks adjacent to the interface. Where figure 5 only shows the latter process, figure 6 clearly demonstrates in which doping combination the former process is dominant. This figure also highlights how the highly
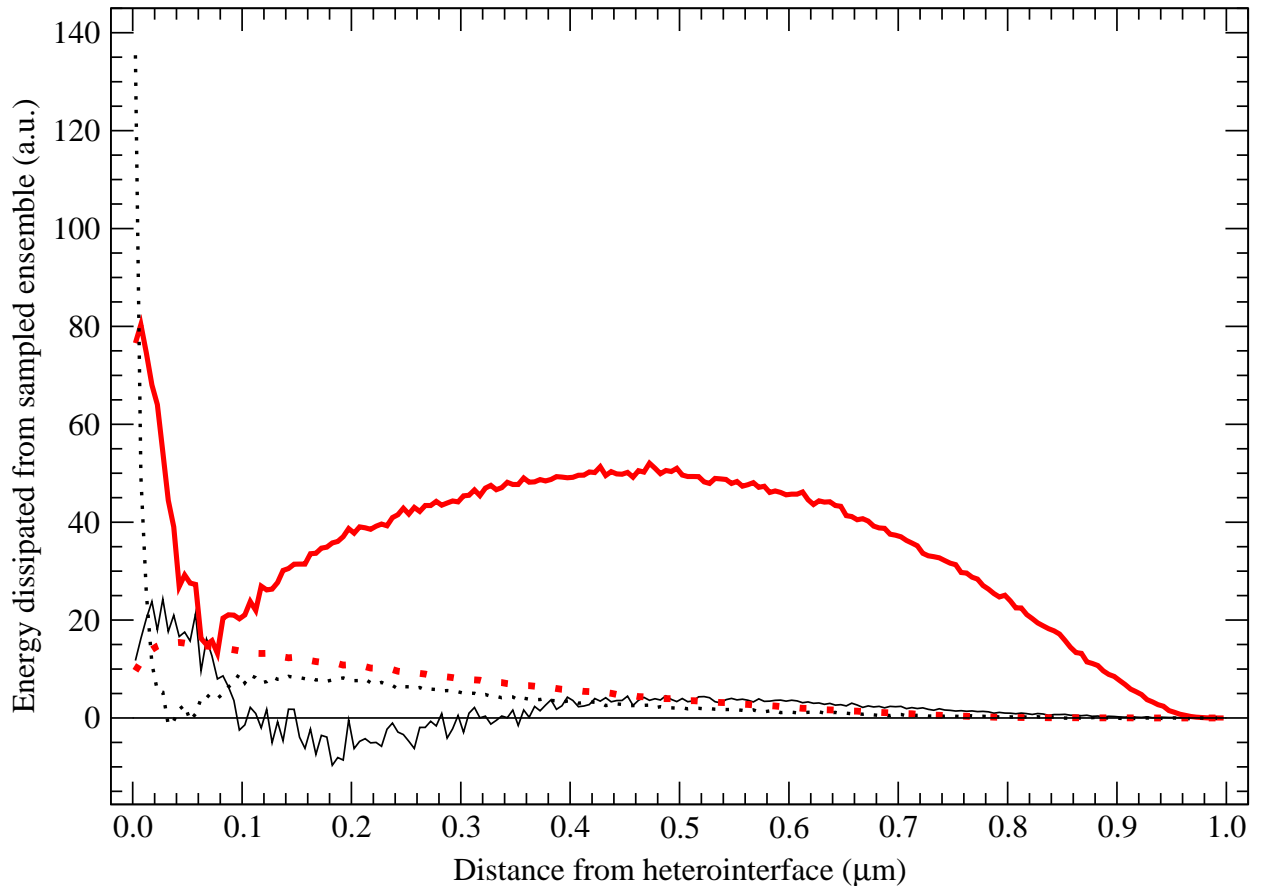

FIG. 5. Spatial histogram of net energy transferred from electrons to lattice via electron-phonon scattering, for the doping type (p-type: dotted, n-type: solid) and density combinations (thick/red: higher doping, thin/black: lower doping) as in figures 3 and 4.

11

doped p-type case has another potential side-effect: the mean energy of electrons entering the Si layer is significantly higher, improving the chances of rapid impact-ionization.
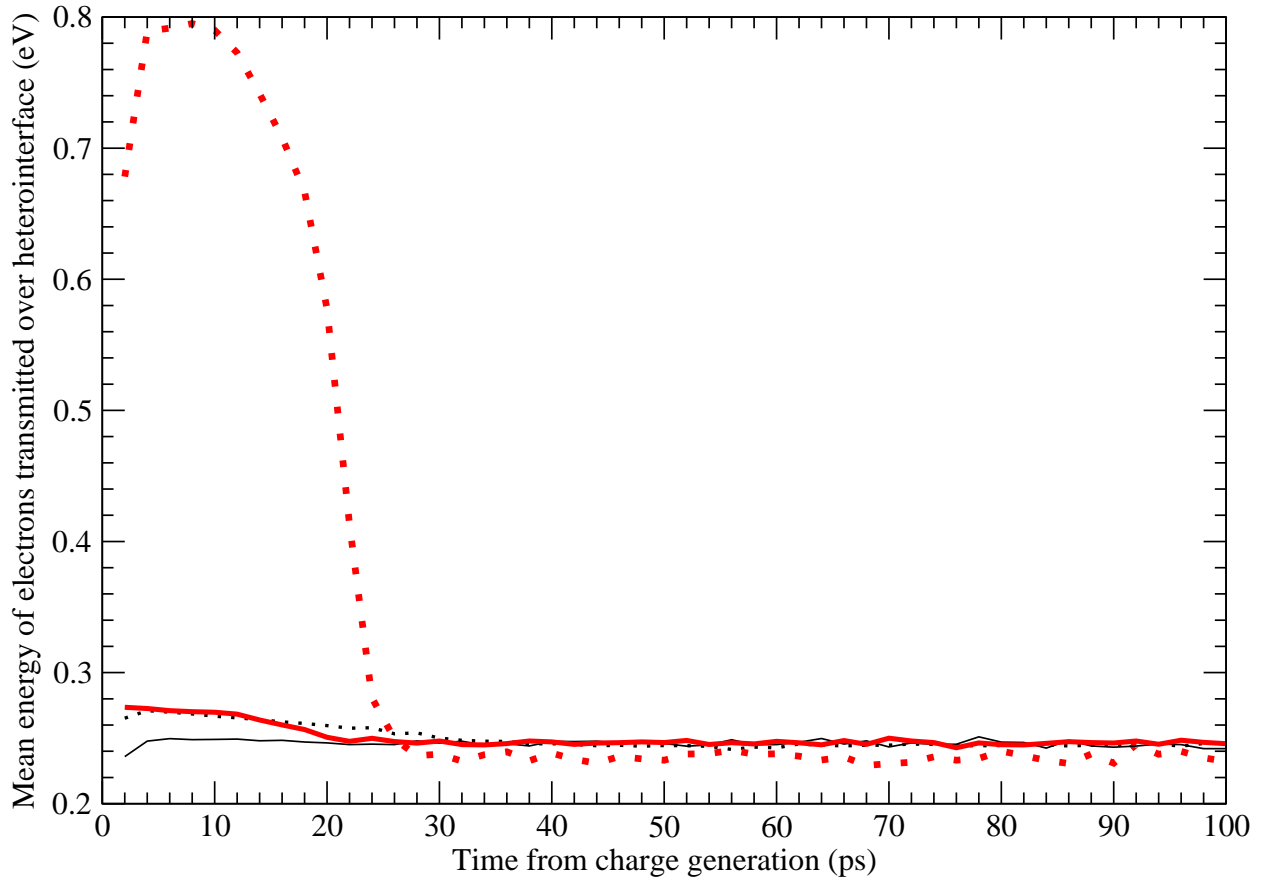

FIG. 6. Mean energy of electrons traversing heterointerface as a function of time, for the doping type (p-type: dotted, n-type: solid) and density combinations (thick/red: higher doping, thin/black: lower doping) of figures 3, 4 and 5. Energy is relative to lowest conduction band minima.

B.   Influence of tunnelling

As stated in section II, two tunnelling mechanisms were considered in addition to the classical transmission over the L state barrier. The effect of including the direct tunnelling on the transmission timescales of figure 4 are shown in figure 7. The degree of tunnelling is parameterised by the electric field in the Si charge layer, the absolute values used in the simulation being a sum of the electric field at the heterointerface according to the Ge layer constraints and the shift over the 0.1 μm charge layer according to equation 1

12

and the Si charge layer doping density (in the triangular barrier approximation). The different thicknesses (colours) of lines in figure 7 therefore allow analysis of the significance of tunnelling for two different Si charge layer doping densities. It is apparent that, for the lower density of Si charge layer doping ($\approx 10^{17}\,\mathrm{cm}^{-3}$) tunnelling has a negligible impact on the transport timescales. For the higher density of Si charge layer doping ($\approx 10^{18}\,\mathrm{cm}^{-3}$), tunnelling has the greatest impact for the cases where the electronic transport is rather slow such as the long time-scale behaviour mentioned in section III A. Even in this case, while the improvement is much more apparent, the effect is not as significant as that which may be achieved by increasing the Ge absorption layer doping density. Higher Si charge layer densities have not been considered, since other device design and processing constraints indicate this is not feasible.

Phonon-assisted tunnelling was found to have even less effect than direct tunnelling, producing an enhancement in Ge to Si transfer probabilities only of the order of a few percent. Given that both tunnelling processes appear to only weakly improve slow-performing cases and have little impact on efficient cases, tunnelling was not included in the calculations described below.

C. Biasing beyond the just-active point

Biasing above the operating point at which the whole Ge layer becomes active leads to a rigid shift in the electric field profile. Given this, applying a higher bias to the cases from figure 4 with low doping will allow the electric field near to the heterointerface to reach the level of that in the p-type high doping case; simulation results which test this idea are shown in figure 8. The top two thin lines are reproductions of the data from figure 4 for low background doping, for n-type (solid) and p-type (dotted) dopants; the lower thin lines are also in pairs and are the result of increasing the electric field profile of these first two lines in steps of $10^6\,\mathrm{V\,m}^{-1}$ each time, as the lines drop towards the bottom left of the figure. While the matching is by no means perfect, and this figure uses a logarithmic scale for the probability, there is a rather good overlap between the p-type (dotted) line from any given set and the n-type (solid) result from the pair at the next higher electric field (closer to the bottom-left). From considering the electric field profiles (similar to figure 3) it is apparent that these very similar lines represent cases where the peak electric field near the
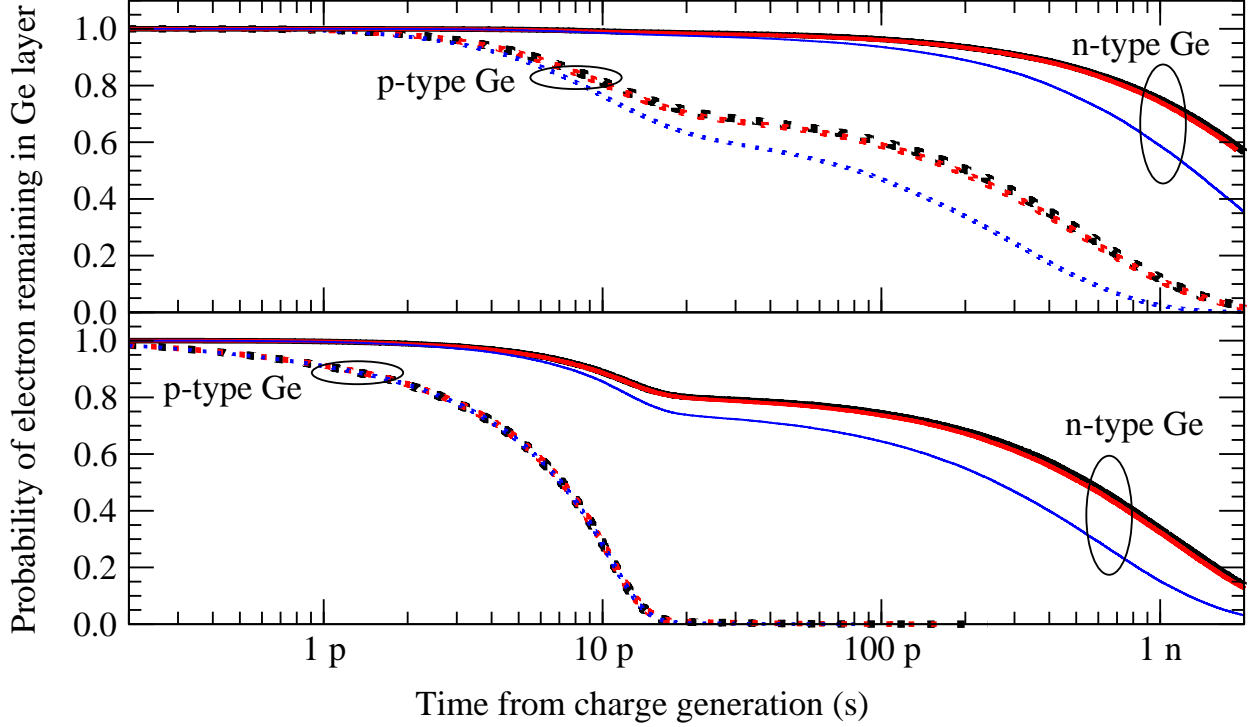
FIG. 7. Probability of a photo-generated electron remaining in a just-active Ge absorption layer as a function of time, and tunnelling barrier electric field. The upper plot is for a peak electric field (doping density) in the Ge layer of $10^6\,\mathrm{V\,m^{-1}}$ ($\approx 10^{15}\,\mathrm{cm^{-3}}$); the lower plot is for $10^7\,\mathrm{V\,m^{-1}}$ ($\approx 10^{16}\,\mathrm{cm^{-3}}$). The thickest (black), thick (red) and thin (blue) lines represent additional electric field variation (as per equation 1) in the Si charge layer of zero (no tunnelling), $10^7\,\mathrm{V\,m^{-1}}$ ($\approx 10^{17}\,\mathrm{cm^{-3}}$) and $10^8\,\mathrm{V\,m^{-1}}$ ($\approx 10^{18}\,\mathrm{cm^{-3}}$) over the 100 nm Si charge layer.

heterointerface is identical. Furthermore, in the bottom-middle of figure 8 it is also clear that two (one solid, one dotted) of these thin lines overlay the thick dotted line, which is a repeat of the high-density p-type result from figure 4. These three results were obtained from simulations with electric field profiles with differing electric field gradients, but all had identical values at the heterointerface. All of this supports the earlier suggestion that the electric field near to the heterointerface is the dominant factor for achieving rapid ($<20\,\mathrm{ps}$) transport timescales.

One additional point evident from figure 8 is that while the just-active high p-type doping case from earlier (figure 4) has 99 % transmission within 20 ps, it also has a long-time tail for the remaining 1 %. This emphasises the dominance of the electric field at the interface in determining the transport-time characteristics, and the possibility of approximating them
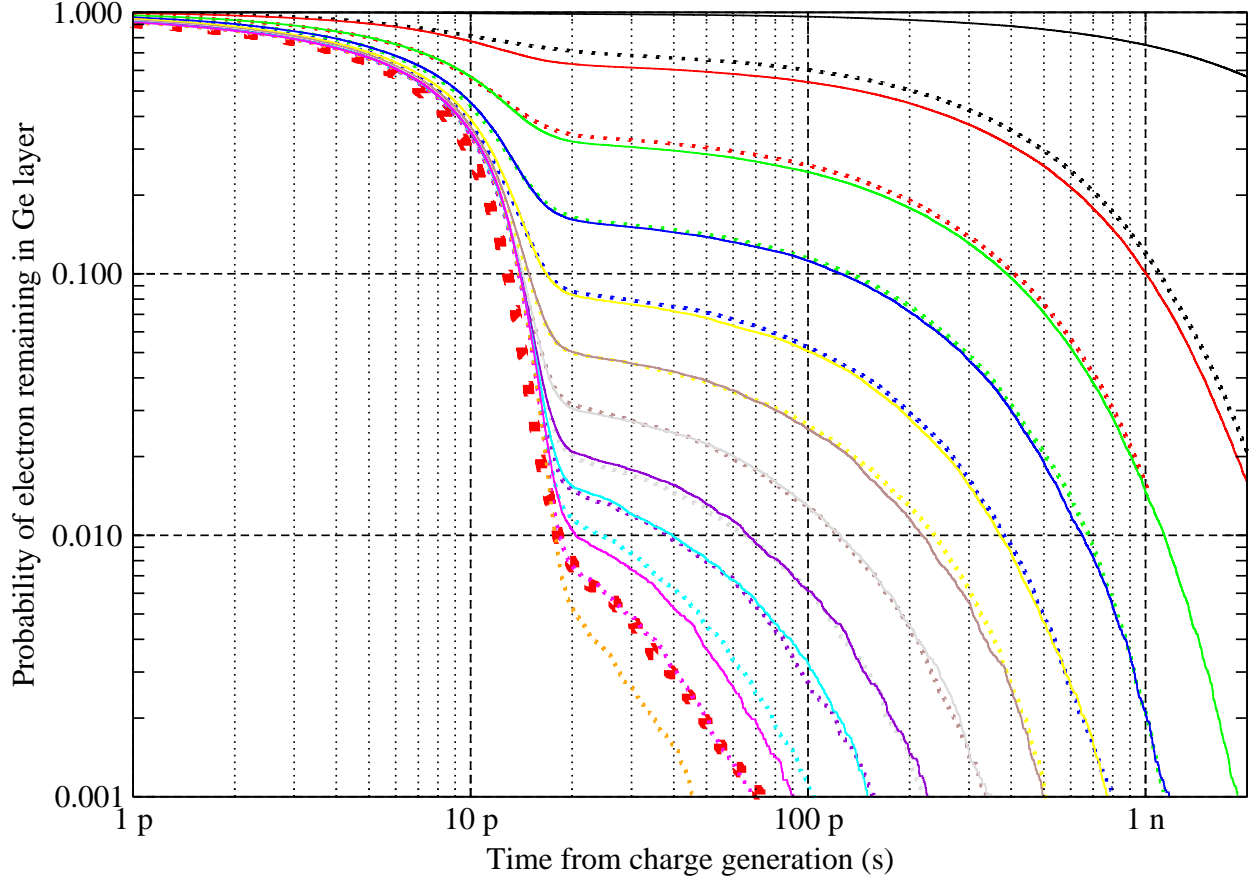
14

FIG. 8. Probability of a photo-generated electron remaining in a just-active Ge absorption layer as a function of time, for various electric field profiles. The thickest dotted (red) line is for p-type doping at a density of $10^{16}\,\mathrm{cm}^{-3}$ (as lowest line in figure 4). The top two thin (black) lines are for n-type (solid) and p-type (dotted) doping at a density of $10^{15}\,\mathrm{cm}^{-3}$ (thin/black lines in figure 4). Pairs of solid and dotted lines (each pair a different colour) below the top two represent increasing the entire electric field profile by $10^6\,\mathrm{V\,m}^{-1}$ for each pair (colour); pairs closer to the thick dotted line correspond to higher electric fields, equivalent to increasing the reverse bias.

through a set of curves indexed by this parameter.

D.   Preferred Ge absorber doping

The results from section III C offer a perspective beyond that of III A, suggesting that as long as the electric field at the interface can be adequately adjusted, through applying a bias beyond the just-active point, then any of the simulated dopant types or densities combined

will suffice. However, this condition only concerns efficient transmission of electrons over the heterointerface; in practice there are various other constraints which must be met in order to achieve SPAD operation.

As indicated in section I, one reason for the SACM (or SAM) design of SPADs is to be able to minimise the electric field in the narrow band-gap material of the absorber layer, so limiting carrier generation and dark current from band-to-band (Zener) tunnelling. While similar transmission characteristics may be obtained for a broad range of uniform dopant type and density combinations so long as the electric field is identical at the heterointerface, the dopant characteristics affect the gradient of the electric field throughout the Ge absorber layer. The band-to-band tunnelling rate increases exponentially with electric field[17], hence p-type background doping in the Ge absorber is preferable to n-type since this results in lower electric fields in the bulk of the layer compared to that at the interface.

According to figures 4 and 8, doping that results in an interfacial electric field of $4 \times 10^6 \, \mathrm{V\,m^{-1}}$ to $10^7 \, \mathrm{V\,m^{-1}}$ should exhibit transmission of $\approx 90\,\%$ to $99\,\%$, respectively, of electrons over the interface within $20\,\mathrm{ps}$ of being photo-generated. For a $1\,\mathrm{\mu m}$ Ge absorption layer to be just-active and meet these criteria would require p-type doping of $4 \times 10^{15} \, \mathrm{cm^{-3}}$ to $10^{16} \, \mathrm{cm^{-3}}$ respectively. Biased appropriately, this simultaneously achieves rapid transport of photogenerated electrons while minimising electric-field-enhanced dark events. A lower background doping density ($4 \times 10^{15} \, \mathrm{cm^{-3}}$) results in a lower internal electric field (hence potentially lower band-to-band tunnelling), but also a lower transport efficiency ($90\,\%$). Through higher reverse biasing, the interfacial electric field may then be raised so as to achieve $99\,\%$ transmission within $20\,\mathrm{ps}$, yet at the cost of increased band-to-band tunnelling. Conversely a higher doping density ($10^{16} \, \mathrm{cm^{-3}}$) results in high transmission in tandem with a minimised internal electric field. Whilst this implies that a higher doping density is preferable, a high *background* doping density is often associated with poor crystalline quality and hence increased dark events.

E.   Jitter calculations

Jitter in a SPAD represents the variability in the delay from photon absorption to the point where a current may be measured, which may be experimentally determined by taking the full width half maximum (FWHM) of the peak in a histogram obtained from a large

number of detection events[1]. Our Monte Carlo simulations can be used to estimate the contribution to jitter due to variations in transit time from the point of photogeneration in the Ge to entry into the Si layer.

The histograms required can be easily calculated by taking the derivative of the transmission time data as presented in figures 4 and 8, leading to results such as in figure 9. An
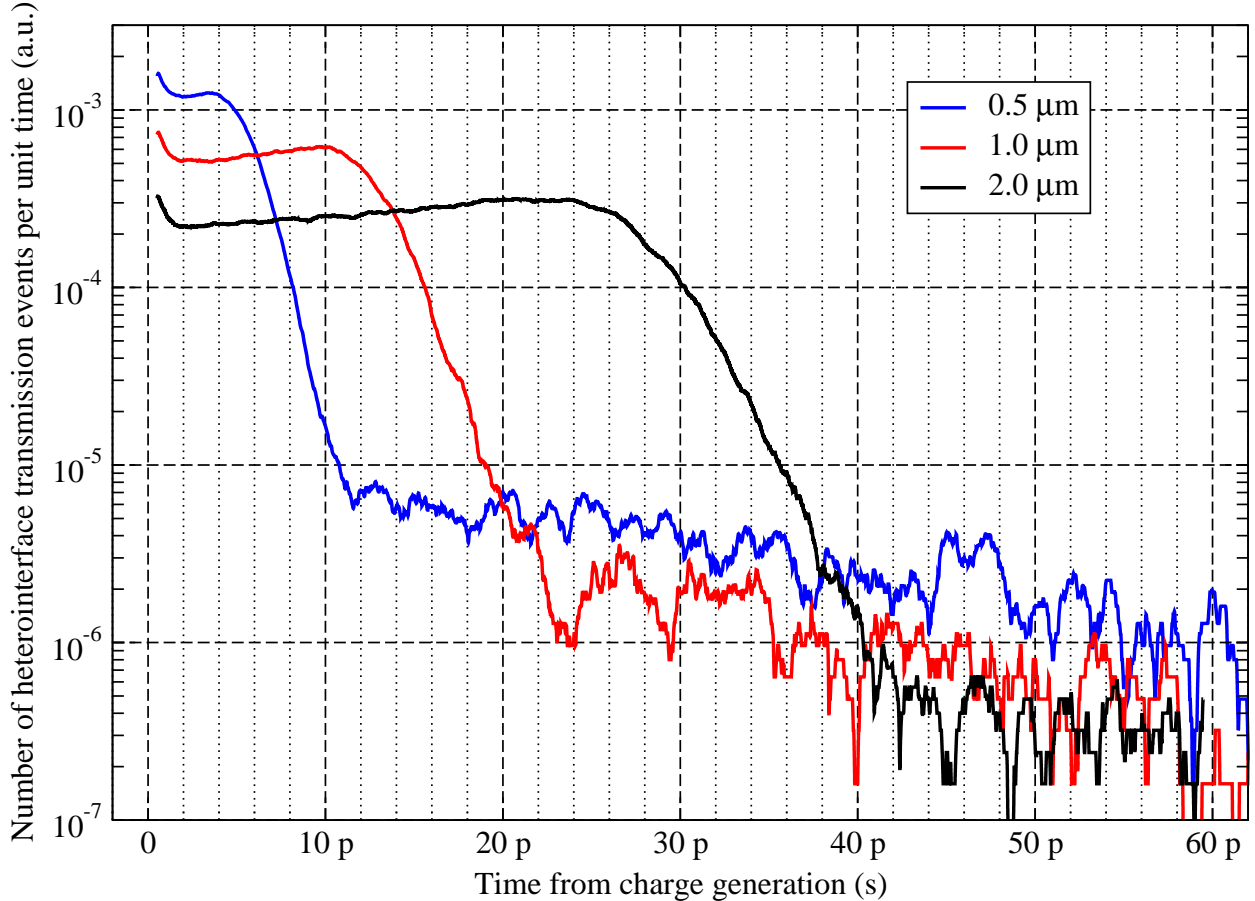

FIG. 9. Histograms of the number of events requiring a given time from charge generation to interfacial transmission, allowing comparison of the contribution to jitter for transport in three different Ge absorber layer heights. Results are for just-active Ge layer conditions, with an electric field of $10^7\,\mathrm{V\,m^{-1}}$ at the heterointerface and zero at the top of the layer, corresponding to uniform p-type doping of $\approx 10^{16}\,\mathrm{cm^{-3}}$ for the $1\,\mu\mathrm{m}$ case, and an appropriately scaled amount for the others according to equation 1. These conditions were selected for comparision since the jitter cannot be determined when the interfacial transport is too low, and does not vary significantly when the transport is rapid.

17

initial rise and later sharp drop (to levels below 10^{-5}) is identifiable for all heights of Ge layer, however each curve typically has two peaks: one at very short times ($< 2\,\mathrm{ps}$) and a later broader one. The former is associated with velocity overshoot of a sub-ensemble of electrons which are generated close to the interface. Selecting either peak for a FWHM measurement does not result in consistent meaningful jitter values.

Jitter values have previously been given for peak heights other than half-maximum[31]; given this precedent we determine limiting values of jitter for a range of histograms similar to those in figure 9. The minimum jitter is calculated by taking the time at which a horizontal line drawn through the minimum between the two peaks intersects the falling edge, while the maximum width is taken as that at which the histogram signal enters the noise. The resulting values for a range of Ge layer heights are shown in figure 10, under the same conditions as in figure 9; understanding the dependence upon absorber height is relevant since this is a future route to improving overall optical absorption and detection efficiency, particularly at longer wavelengths. The shaded region is obtained by approximate linear fits of the limiting values and reproduces the simulation results remarkably well. The upper bound passes very close to the origin, indicating the good quality of the data and linear fit. The fit lower bound intercepts the horizontal axis at $0.25\,\mu\mathrm{m}$, for which simulations confirm that the two peaks merge, supporting the prediction from the fit that this bound approaches zero. With a single peak the standard FWHM jitter may be determined and was found to be $1.57\,\mathrm{ps}$.

The relative significance of the jitter components determined above will vary according to other jitter contributions in the system. These could include those due to the multiplication process itself[32,33], including expansion of the current filament[34], or those external to the active device. For thick Ge absorption layers the contribution to jitter from the processes modelled here could become significant in otherwise low-jitter designs[1] or operating conditions[34].

IV. CONCLUSIONS

Monte Carlo electronic transport simulations have been employed to analyse the impact of Ge absorber doping on performance characteristics of Ge/Si SPADs. Doping directly influences the electric field gradient but it is the electric field adjacent to the heterointerface
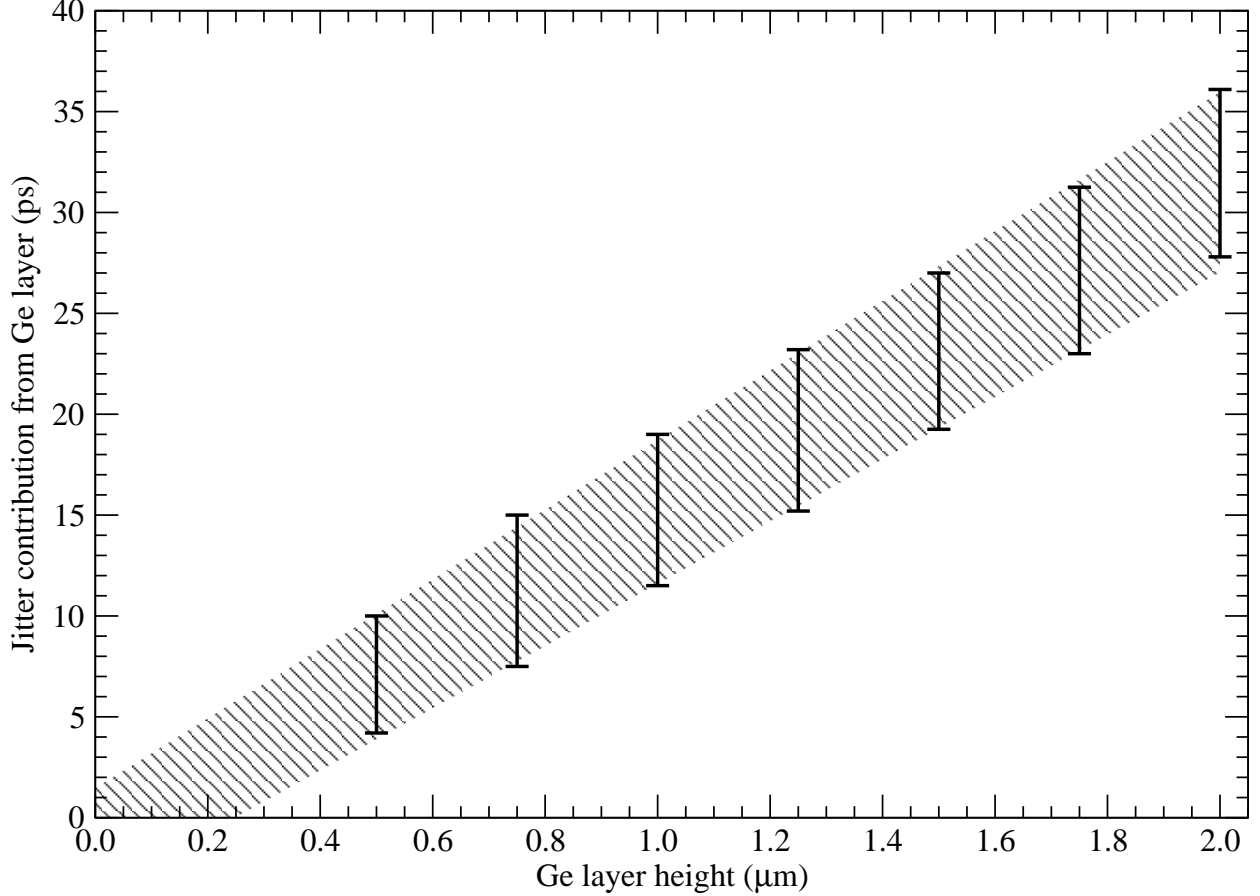
FIG. 10. Estimated range of jitter for various Ge absorber layer heights. The shaded band represents the range of jitter values between these limits, using a linear fit for the upper and lower bound.

which is found to be the dominant factor in minimising the time that photo-generated electrons spend in the Ge. Nevertheless, p-type doping is preferable to n-type, since it allows the device to be biased such that the electric field is high enough at the Ge/Si interface to achieve rapid electron transfer into the Si layer, yet which is low enough elsewhere to minimise dark events from tunnelling. The ideal density of p-type dopants for rapid charge transport varies according to the height of the Ge absorber layer; for a $1\,\mu m$ thick layer as primarily analysed here, a density of $\approx 4 \times 10^{15}\,cm^{-3}$ to $1 \times 10^{16}\,cm^{-3}$ should achieve a transport efficiency of $90\,\%$ to $99\,\%$ respectively within $20\,ps$, when the layer is just-active. Higher efficiencies will occur as the bias is raised, at the cost of increased dark events from tunnelling and the potential for breakdown to occur in the Ge rather than the Si layer. These doping densities are in the likely range of background doping in the Ge absorber

layer. However, if the background doping is n-type, it may be desirable to compensate this with identical p-type doping in order to achieve the optimum electric field profile described above.

The contribution to jitter from the Ge/Si heterointerface is difficult to ascertain, but does not appear to vary significantly with bias or doping for conditions under which devices are expected to function. The jitter contribution varies linearly with the Ge absorber layer height and the estimated minimum jitter approaches 27 ps for a 2 µm high Ge absorber layer, which is of the same order of magnitude as the minimum jitter found in some experimental devices[34].

ACKNOWLEDGMENTS

REFERENCES

[1] G. S. Buller and R. J. Collins, Measurement Science and Technology **21**, 012002 (2010).

[2] E. Knill, R. Laflamme, and G. J. Milburn, Nature **409**, 46 (2001).

[3] C. H. Bennett and G. Brassard (Bangalore, India, 1984) pp. 175–179.

[4] S. Bellis, C. Jackson, and A. König, Laser+Photonik , 34 (2005).

[5] J. S. Massa, A. M. Wallace, G. S. Buller, S. J. Fancey, and A. C. Walker, Optics Letters **22**, 543 (1997).

[6] A. Tosi, F. Stellari, A. Pigozzi, G. Marchesi, and F. Zappa, in *Reliability Physics Symposium Proceedings, 2006. 44th Annual., IEEE International* (2006) pp. 595 –601.

[7] S. Cova, M. Ghioni, A. Lacaita, C. Samori, and F. Zappa, Applied Optics **35**, 1956 (1996).

[8] B. F. Levine, C. G. Bethea, and J. C. Campbell, Electronics Letters **20**, 596 (1984).

[9] Y. Maruyama and E. Charbon, in *Solid-State Sensors, Actuators and Microsystems Conference (TRANSDUCERS), 2011 16th International* (2011) pp. 1180 –1183.

[10] S. Assefa, F. Xia, and Y. A. Vlasov, Nature **464**, 80 (2010).

[11] Y. Kang, H.-D. Liu, M. Morse, M. J. Paniccia, M. Zadka, S. Litski, G. Sarid, A. Pauchard, Y.-H. Kuo, H.-W. Chen, W. S. Zaoui, J. E. Bowers, A. Beling, D. C. McIntosh, X. Zheng, and J. C. Campbell, Nat Photon **3**, 59 (2009).

[12] P. C. M. Owens, J. G. Rarity, P. R. Tapster, D. Knight, and P. D. Townsend, Applied Optics **33**, 6895 (1994).

[13] A. Lacaita, P. A. Francese, F. Zappa, and S. Cova, Applied Optics **33**, 6902 (1994).

[14] Z. Zhou, C. Li, H. Lai, S. Chen, and J. Yu, Journal of Crystal Growth **310**, 2508 (2008).

[15] V. Shah, A. Dobbie, M. Myronov, and D. Leadley, Solid-State Electronics **62**, 189 (2011).

[16] V. M. Robbins, T. Wang, K. F. Brennan, K. Hess, and G. E. Stillman, Journal of Applied Physics **58**, 4614 (1985).

[17] D. A. Ramirez, M. M. Hayat, and M. A. Itzler, IEEE Journal of Quantum Electronics **44**, 1188 (2008).

[18] C. Jacoboni and L. Reggiani, Reviews of Modern Physics **55**, 645 (1983).

[19] N. J. Pilgrim, W. Batty, and R. W. Kelsall, Journal of Computational Electronics **1**, 263 (2002).

[20] T. Sadi, R. Kelsall, and N. Pilgrim, IEEE Transactions on Electron Devices **53**, 1768 (2006).

[21] N. J. Pilgrim, A. Khalid, G. M. Dunn, and D. R. S. Cumming, Semiconductor Science and Technology **23**, 075013 (2008).

[22] N. J. Pilgrim, A. Khalid, C. Li, G. M. Dunn, and D. R. S. Cumming, physica status solidi (c) **8**, 313 (2011).

[23] C. Jacoboni, F. Nava, C. Canali, and G. Ottaviani, Physical Review B **24**, 1014 (1981).

[24] G. H. Li, A. R. Goñi, K. Syassen, and M. Cardona, Physical Review B **49**, 8017 (1994).

[25] C. G. Van de Walle and R. M. Martin, Physical Review B **34**, 5621 (1986).

[26] J. Liu, D. D. Cannon, K. Wada, Y. Ishikawa, D. T. Danielson, S. Jongthammanurak, J. Michel, and L. C. Kimerling, Physical Review B **70**, 155309 (2004).

[27] M. Rouvière, M. Halbwax, J.-L. Cercus, E. Cassan, L. Vivien, D. Pascal, M. Heitzmann, J.-M. Hartmann, and S. Laval, Optical Engineering **44**, 075402 (2005).

[28] T. González and D. Pardo, Solid-State Electronics **39**, 555 (1996).

[29] M. M. Rieger and P. Vogl, Physical Review B **48**, 14276 (1993).

[30] E.-j. Bai and Q.-q. Shu, Chinese Physics Letters **15**, 862 (1998).

[31] P. J. Clarke, R. J. Collins, P. A. Hiskett, M.-J. García-Martínez, N. J. Krichel, A. Mc-

Carthy, M. G. Tanner, J. A. O'Connor, C. M. Natarajan, S. Miki, M. Sasaki, Z. Wang, M. Fujiwara, I. Rech, M. Ghioni, A. Gulinatti, R. H. Hadfield, P. D. Townsend, and G. S. Buller, New Journal of Physics **13**, 075008 (2011).

[32]S. L. Tan, D. S. Ong, and H. K. Yow, Journal of Applied Physics **102**, 044506 (2007).

[33]D. Dolgos, H. Meier, A. Schenk, and B. Witzigmann, Journal of Applied Physics **110**, 084507 (2011).

[34]M. Assanelli, A. Ingargiola, I. Rech, A. Gulinatti, and M. Ghioni, IEEE Journal of Quantum Electronics **47**, 151 (2011).

p+		contact
i Ge	1 μm	optical absorber
p	0.1 μm	charge layer
i Si	1 μm	charge multiplier
n+		contact

E-field